

PAPER • OPEN ACCESS


High-uniformity atomic layer deposition of superconducting niobium nitride thin films for quantum photonic integration

To cite this article: C T Lennon *et al* 2023 *Mater. Quantum. Technol.* **3** 045401

View the [article online](#) for updates and enhancements.

You may also like

- [Fiber-coupled quantum light sources based on solid-state quantum emitters](#)
Lucas Bremer, Sven Rodt and Stephan Reitzenstein
- [A Silicon Shallow-Ridge Waveguide Integrated Superconducting Nanowire Single Photon Detector Towards Quantum Photonic Circuits](#)
Lingjie Yu, , Heqing Wang et al.
- [Improvement of critical temperature of niobium nitride deposited on 8-inch silicon wafers thanks to an AlN buffer layer](#)
Raouia Rhazi, Houssaine Machhadani, Catherine Bougerol et al.

 **kiutra**

Easy-to-use and Helium-3 free
cryogenics solutions

LEARN MORE

Materials for Quantum Technology



PAPER

High-uniformity atomic layer deposition of superconducting niobium nitride thin films for quantum photonic integration

OPEN ACCESS

RECEIVED
20 July 2023

REVISED
11 October 2023

ACCEPTED FOR PUBLICATION
8 November 2023

PUBLISHED
20 November 2023

Original content from this work may be used under the terms of the [Creative Commons Attribution 4.0 licence](#).

Any further distribution of this work must maintain attribution to the author(s) and the title of the work, journal citation and DOI.



C T Lennon^{1,*} , Y Shu² , J C Brennan¹ , D K Namburi¹ , V Varghese¹, D T Hemakumara², L A Longchar³ , S Srinath³  and R H Hadfield¹ 

¹ James Watt School of Engineering, University of Glasgow, University Avenue, Glasgow G12 8QQ, United Kingdom

² Oxford Instruments Plasma Technology, North End, Bristol BS49 4AP, United Kingdom

³ School of Physics, University of Hyderabad, Hyderabad 500 046, India

* Author to whom any correspondence should be addressed.

E-mail: c.lennon.1@research.gla.ac.uk

Keywords: atomic layer deposition, superconducting thin films, niobium nitride, superconducting quantum detectors, quantum photonics

Abstract

Atomic layer deposition (ALD) has been identified as a promising growth method for high-uniformity superconducting thin films for superconducting quantum photonic applications, offering superior uniformity, thickness control and conformality to techniques such as reactive sputtering. The potential scalability of ALD makes this method especially appealing for fabrication of superconducting nanowires and resonators across large areas. We report on the growth of highly uniform superconducting NbN thin films via plasma-enhanced atomic layer deposition (PEALD) with radio frequency substrate biasing, on a 200 mm (8 inch) Si wafer, specifically for superconducting nanowire single-photon detector applications. Niobium nitride films were grown using (tert-butylimido)-tris(diethylamido)-niobium(V) precursor and an H₂/Ar plasma. The superconducting properties of a variable thickness series of films (5.9–29.8 nm) show critical temperature (T_c) of 13.5 K approaching bulk thickness (28.8 nm) with low suppression down to the ultrathin regime (5.9 nm), with $T_c = 10.2$ K. T_c across the 200 mm wafer with 8 nm thick NbN, measured in 15 mm intervals, exhibits minimal variation (<7%). Microbridge structures fabricated on 8 nm thick NbN films also exhibit high critical current densities (J_c), > 10 MA cm⁻² at 2.6 K. PEALD could therefore be a pivotal technique in enabling large-scale fabrication of integrated quantum photonic devices across a variety of applications.

1. Introduction

Atomic layer deposition (ALD) is a subclass of chemical vapour deposition, relying on the sequential and self-limiting exposure of gaseous precursor species, forming a single atomic layer of material [1]. This process, known as the ‘ALD cycle’, can then be repeated until a desired thickness is attained, enabling Ångstrom-level thickness control [2]. ALD is therefore highly uniform, conformal and scalable, with the deposition area being limited by the size of the reaction chamber [3, 4]. Consequently, there has been significant interest from the superconducting device community, where uniform, pinhole-free films are a necessity for applications such as superconducting nanowire single-photon detectors (SNSPDs), microwave kinetic inductance detectors (MKIDs), superconducting resonators, superconducting qubits and superconducting through-silicon vias [5–9]. For MKIDs and SNSPDs in particular, large area uniformity is essential for scaling up to large area arrays and cameras [10].

SNSPDs are the gold standard in single-photon detection, offering unparalleled detection efficiency, timing resolution and spectral range [11]. Recent studies utilising SNSPDs made from refractory metal nitride thin films have shown >99% system detection efficiency at telecom wavelengths and sub-3 ps temporal resolution for visible wavelengths [12, 13]. Highly uniform, homogenous thin films are a necessity for SNSPDs, as constrictions and film inhomogeneities actively suppress the critical current of the nanowire,

leading to reduced timing resolution and detection efficiency, therefore necessitating operation at lower temperatures [14]. NbN thin films for SNSPDs have typically been deposited using reactive magnetron sputtering of Nb metal with N₂ gas, however, sputtering struggles to produce uniform, pinhole-free films over large areas, being limited due to its line-of-site nature and requirement of high temperatures [15, 16]. Consequently, ALD of metal nitrides has received significant interest in recent years, with several studies showcasing films with high T_c and J_c , essential for the fabrication of high efficiency, high temporal resolution SNSPDs [17–20]. This success has largely been enabled by utilising a plasma-enhanced atomic layer deposition (PEALD) process, as conventional thermal ALD of superconducting metal nitrides requires metal chloride based precursors, which can lead to low-level chlorine incorporation in the film, resulting in device corrosion [21]. There have been several studies reporting the fabrication of SNSPDs using PEALD NbN films, exhibiting single-photon sensitivity up to 2.1 μm [22, 23]. This has demonstrated the power of PEALD for SNSPD applications, but there is still much improvement on growth optimisation to be made to realise its full potential. In this study, superconducting NbN thin films have been grown using PEALD over large area (200 mm). Their superconducting, electrical and structural properties have been examined, with suitability for fabrication of large-area SNSPDs assessed and discussed.

2. Methods

ALD NbN films were grown at Oxford Instruments Plasma Technology, Bristol, on an FlexAL system, equipped with radio frequency (RF) substrate biasing, using (tert-butylimido)-tris(diethylamido)-niobium(V) (TBTDEN) precursor with an Ar/H₂ plasma. High resistivity (>10 k Ω cm) <100> Si substrates, cleaned using organic solvents, were used for the film growth, with a deposition temperature of 250 °C. A thickness series (target thicknesses: 5, 8, 15, 20 and 30 nm) was grown to elucidate the relationship between film thickness (d), sheet resistance (R_s) and T_c . Film thickness was verified using a J A Woollam M-2000 spectroscopic ellipsometer. Deposition across 200 mm Si wafer followed the same process detailed for the thickness series, with the thickness uniformity across the sample measured using ellipsometry, as shown in figure 1(a). Surface roughness measurements were performed using a Bruker dimension icon atomic force microscope (AFM), used in non-contact mode for high resolution, with a scan speed of 0.1 $\mu\text{m s}^{-1}$. X-ray diffraction (XRD) studies were performed at the University of Hyderabad, School of Physics, in a Bruker D8 DISCOVER x-ray diffractometer with a Cu K- α source, used in grazing incidence mode due to the thickness of the samples. The scan angle 2θ -range was 20°–80°, with an incidence angle, ω , of 0.6°. Rietveld refinement on the diffraction patterns were performed using the Profex software package [24]. The T_c of each sample was measured using a standard four-probe resistance measurement technique, housed in a cryogen free closed cycle cooling system, designed and built in-house based on a Sumitomo RDK-101D Gifford-McMahon coldhead and Sumitomo CNA-11C compressor. The system uses pogo pins as electrical contacts and is capable of testing up to eight samples simultaneously down to 2.2 K, with the system equipped with radiation and magnetic shielding at the sample stage. Four-probe resistance measurements were performed using a Stanford Research Systems SIM928 isolated voltage source and SIM970 digital voltmeter. J_c measurements were performed in the same setup, with the samples being modified by photolithography and reactive ion etching to create a microbridge structure from which J_c can be derived, with all fabrication performed at the James Watt Nanofabrication Centre (University of Glasgow). The photolithography process was done with S1805 photoresist etch mask, using a SUSS MicroTec MA6 optical mask aligner. Reactive ion etch was performed using an Oxford Instruments Plasma Lab 80+ tool, using an SF₆/N₂ etch chemistry. Transmission electron microscopy (TEM) studies were performed at the Kelvin Nanocharacterisation Centre (University of Glasgow, School of Physics), using a JEOL ARM200cF in scanning (STEM) mode, with sample preparation done using a standard focused ion beam lift-out technique [25].

3. Results and discussion

3.1. Superconducting and electrical properties of ALD NbN thin films

Figure 1(b) shows the measured film thickness, d , versus the number of ALD cycles, with a deposition rate of 0.20 Å cycle⁻¹. It should be noted that thickness estimation using spectroscopic ellipsometry on ultrathin films has intrinsic limitations, primarily from overfitting. Consequently, we have further verified thickness using TEM. Figure 1(c) shows sheet resistance (R_s) and resistivity (ρ) versus number of cycles. R_s is defined by the equation $R_s = R\alpha\pi(\ln(2))^{-1}$, where R is the measured resistance and α is a geometrical correction factor related to the substrate size and probe geometry [26]. ρ is calculated by multiplying R_s by d . The relationship between ρ and d indicates an improved crystallinity with increasing film thickness, with ρ decreasing with increasing film thickness by 54.6% from $d = 5.9$ nm to $d = 29.8$ nm. In the ultrathin regime (5.9 nm), ρ of 210 $\mu\Omega$ cm shows good agreement to values reported in the literature for other NbN PEALD

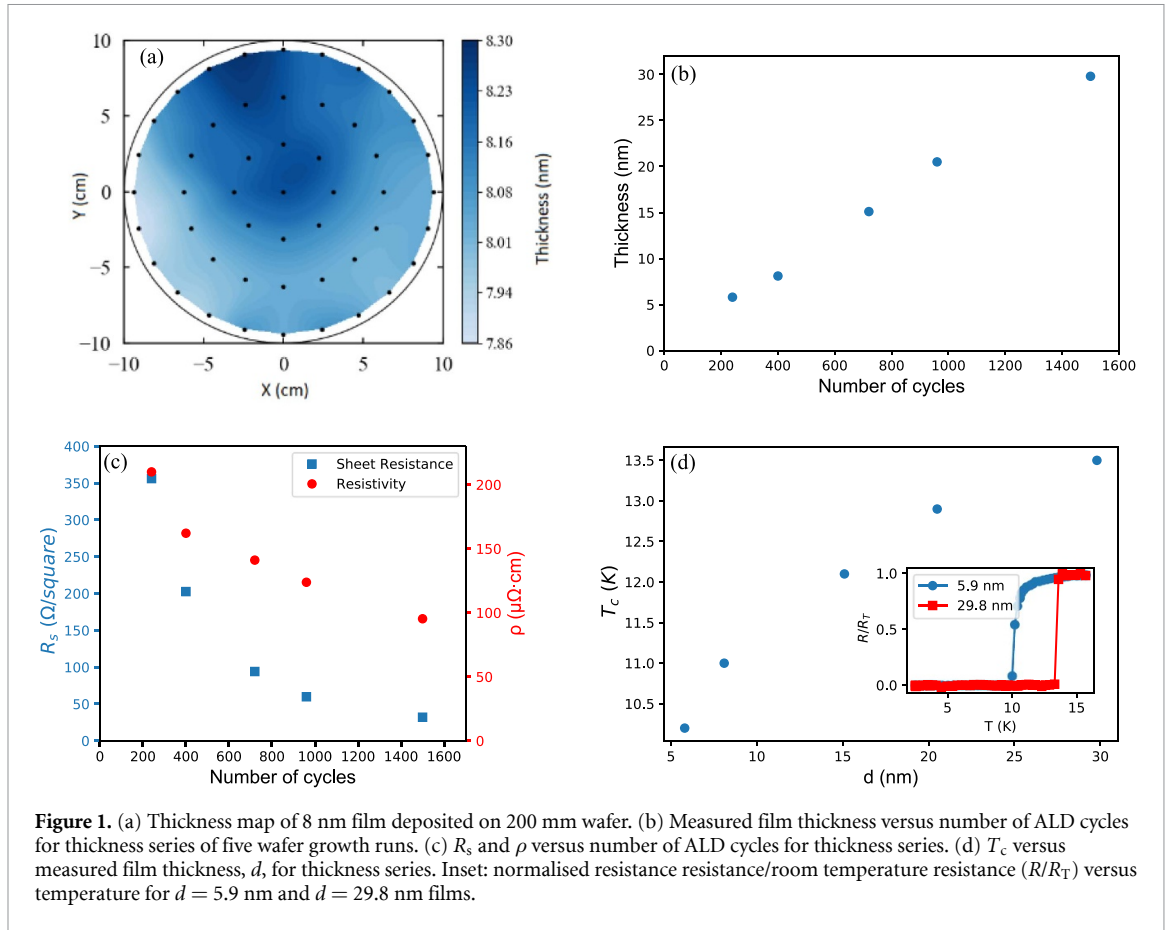


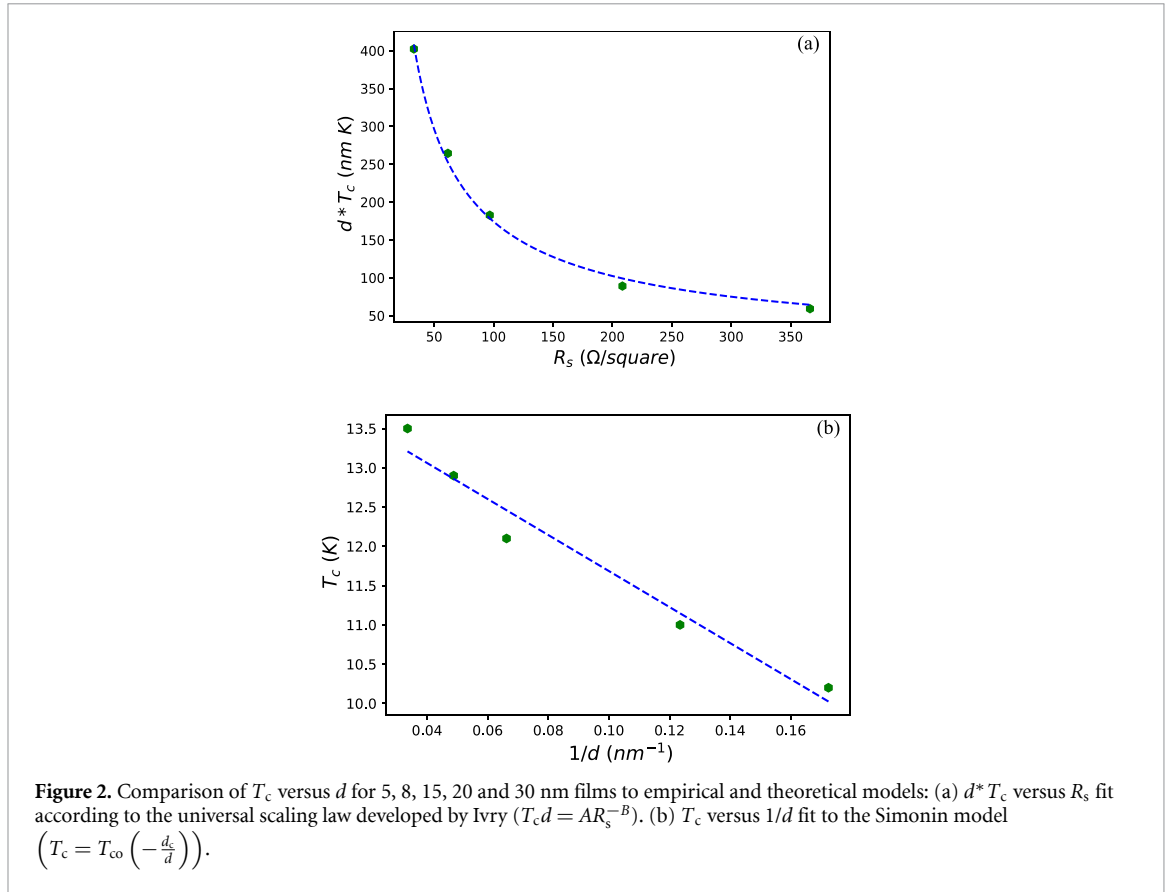
Figure 1. (a) Thickness map of 8 nm film deposited on 200 mm wafer. (b) Measured film thickness versus number of ALD cycles for thickness series of five wafer growth runs. (c) R_s and ρ versus number of ALD cycles for thickness series. (d) T_c versus measured film thickness, d , for thickness series. Inset: normalised resistance resistance/room temperature resistance (R/R_T) versus temperature for $d = 5.9$ nm and $d = 29.8$ nm films.

Table 1. Summary of superconducting and electrical properties for ALD NbN thickness series detailed in figure 1.

Measured film thickness, d (nm)	Number of ALD cycles	R_s (Ω/\square)	RRR	ρ ($\mu\Omega\cdot\text{cm}$)	T_c (K)	ΔT_c (K)
5.9	240	356.13	1.01	210.0	10.2	0.9
8.0	400	202.65	1.02	162.1	11.0	0.8
15.0	720	94.08	1.06	141.1	12.1	0.6
20.7	960	59.82	1.07	123.8	12.9	0.3
29.8	1500	31.99	1.02	95.3	13.5	0.3

process used for the fabrication of SNSPDs, with ρ in the thicker regime being significantly lower and indicating a more metallic, crystalline film [18]. The residual resistance ratio (RRR) of each sample was also determined, defined as the ratio of resistance at 290 K to resistance just above the transition temperature. RRR can be used to infer the conducting or insulating nature of the film, as well as the crystal quality and film purity [19, 27]. The RRR values of the ALD NbN films grown for the thickness series are all ~ 1 , with minimal change with increasing thickness ($< 7\%$). Table 1 displays the RRR value for each film. Notably, the RRR for these NbN films is significantly higher than those reported in previous studies grown via PEALD (0.64–0.73) [19], indicating a more metallic, crystalline and homogeneous film.

The superconducting properties of the thickness series are summarised in table 1. T_c as a function of d is shown in figure 1(d). T_c is defined as the midpoint between the temperature at $0.9R_{20K}$ and $0.1R_{20K}$, with the superconducting transition width, ΔT_c , taken as the temperature difference between $0.9R_{20K}$ and $0.1R_{20K}$. T_c follows the expected relationship, increasing as film thickness increases, and close to saturating at 13.5 K for $d = 29.8$ nm. T_c in the ultrathin regime (< 10 nm) is measured as 10.2 K (5.9 nm) and 11.0 K (8.0 nm), showing good potential for SNSPD fabrication and agreement with literature-high values for previously documented PEALD and sputtering processes [3, 6, 28]. Notably, our films show higher T_c compared to sputtered films grown on Si and Si with an AlN buffer layer, with T_c of 8.1 K and 10.3 K, respectively, for $d = 9$ nm [29]. ΔT_c is an insightful parameter for investigating the homogeneity of superconducting thin films, as it considers the variation in T_c across multiple areas of the film, whereas T_c itself is dominated by any adjacent, high-quality area of NbN. We see an increase in ΔT_c with decreasing $d > 50\%$ going from $d = 29.8$ nm to $d = 5.9$ nm. This is expected given the previously mentioned relationship between R_s and ρ



to d . Again, we show superior ΔT_c compared to sputtered films grown on Si and Si with AlN buffer: 0.8 K for PEALD versus 1.4 K for sputtering [29].

Elucidating the relationship between T_c and film thickness is paramount to the design of various superconducting technologies, with the drop-off in T_c as the film thickness approaches the coherence length being well documented and understood [30]. We consequently compare the observed relationship between T_c and film thickness to established empirical and theoretical models. Ivry *et al* proposed an empirical universal scaling law for films at the superconductor–insulator transition that relates d and R_s to T_c [30]. The model shows that T_c and d scale proportionally with R_s , resulting in the following power law:

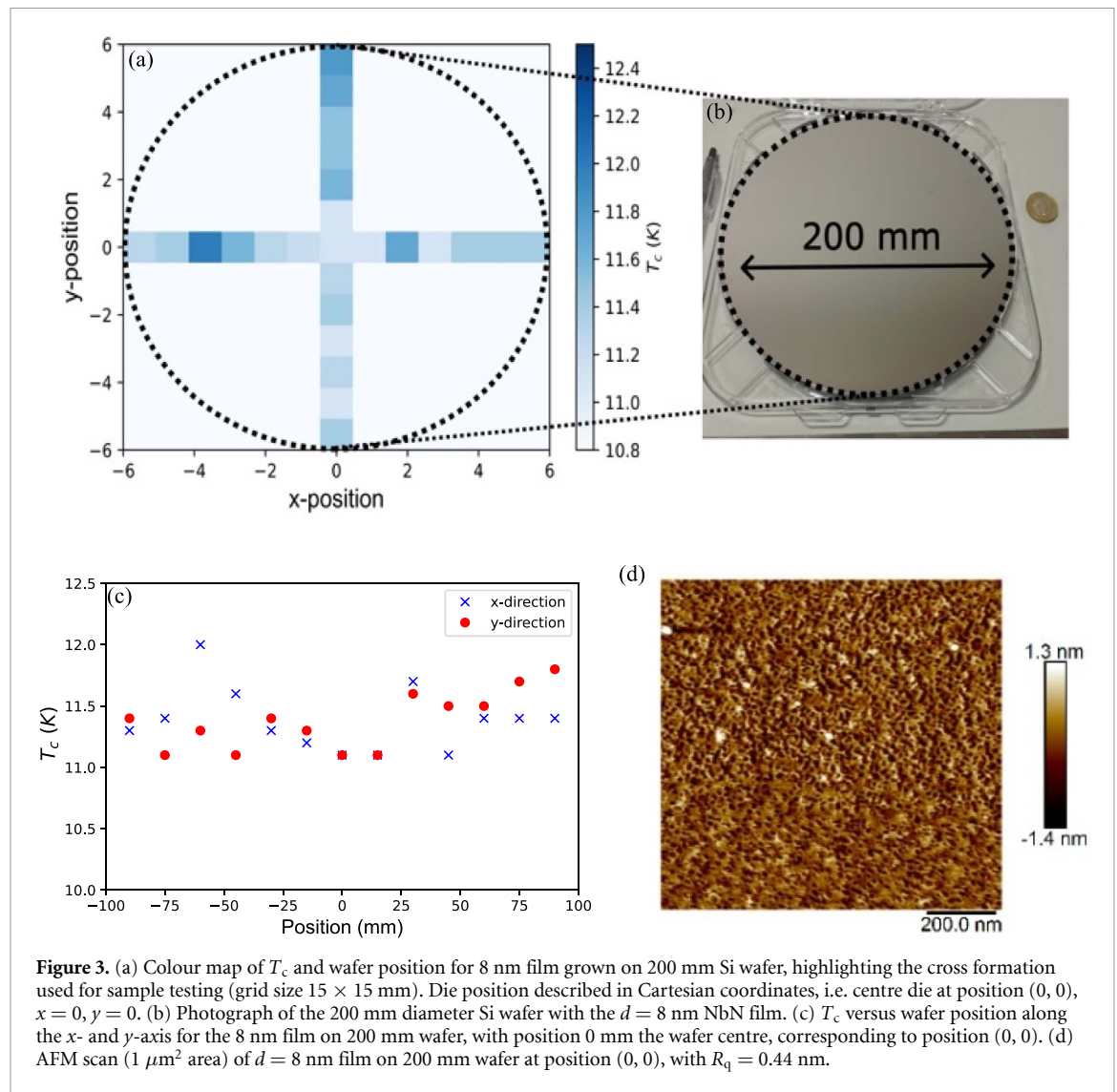
$$T_c d = AR_s^{-B} \quad (1)$$

where A and B are independent fitting parameters. Figure 2(a) shows $T_c \cdot d$ versus R_s , measured for the thickness series, with the data fitted to equation (1) using a nonlinear least squares method. Extracted values for the fitting parameters are: $A = 5934.39 \pm 836.02$, $B = 0.77 \pm 0.03$. Fitting parameter B was shown by Ivry *et al* to relate to film disorder, with amorphous films having $B > 1$. From the historical analysis by Ivry *et al* of several sputtered NbN thin film studies, the extracted B values range from 0.85 to 1.06. Consequently, we can show that the films in this study exhibit less disorder, indicating PEALD can produce a more crystalline film with fewer defects/impurities. Figure 2(a) clearly shows a good agreement between the observed data and the scaling law model.

A simple theoretical model of thin film superconductivity was introduced by Simonin, based on the Ginzburg–Landau theory, which relates d and T_c [31]. The resulting relation is given by:

$$T_c = T_{co} \left(1 - \frac{d_c}{d}\right) \quad (2)$$

where T_{co} is the bulk superconducting transition temperature (16 K for NbN) and fitting parameter d_c is the critical thickness. d_c is defined as the thickness at which there is a complete breakdown in the superconducting phase, below which superconductivity will not be observed. Figure 2(b) shows the measured T_c vs $1/d$ with the data fitted to equation (2). The extracted d_c from the fitting procedure is $1.6 \text{ nm} \pm 0.16$, with T_{co} of $13.98 \text{ K} \pm 0.27$. This indicates that for $d = 29.8 \text{ nm}$, where we have measured $T_c = 13.5 \text{ K}$, we are approaching the expected theoretical limit of T_c ($\sim 14 \text{ K}$) for this NbN PEALD process, which is confirmed by the emergence of a plateau in figure 1(d) as film thickness increases.



3.2. Uniformity of ALD NbN process across 200 mm wafer

To examine the uniformity of our PEALD NbN process in the ultrathin film regime, we diced the 8 nm thick sample grown on a 200 mm diameter Si wafer, shown in figure 3(b), into 15×15 mm dies compatible with our low temperature electrical testing setup. We tested samples positioned in a cross formation along the wafer: 13 samples along both the x - and y -axes crossing the wafer centre, with the variation in T_c across the wafer shown in figures 3(a) and (c). The variation in T_c , R_s and ΔT_c with respect to wafer position are summarised in table 2. We observe minimal variation in the superconducting properties across the wafer, with the maximum variation in T_c of 9.1%, with the maximum $T_c = 12.0$ K (position $(-4, 0)$) and minimum $T_c = 11.1$ K (position $(0, 0)$). The maximum variation in T_c from wafer centre to wafer edge (90 mm range) = 6.3%. This is consistent with the measured variation in R_s from wafer centre to edge of -9.9% . This shows an improvement from a previous study by Knehr *et al*, where they observe a 10% variation in T_c over a 50 mm range [17]. In that study they attribute drop-off in the T_c primarily to a decrease in lattice parameter from 4.37 to 4.31 Å, coming into effect at a 40 mm range from the wafer centre. It is posited that the plasma source used in the Oxford Instruments Plasma Technology OpAL ALD system, where the plasma is generated from a small inductively coupled plasma tube with 65 mm diameter, is the primary factor in the observed drop-off. The plasma source for the FlexAL tool is identical in geometry, therefore we would expect a similar effect in our films. In this study, however, we have utilised RF substrate biasing during the ALD cycles, which has been reported to modulate the electrical and structural properties of thin films [32]. The role of plasma generated ions has been shown to improve crystallinity in metal nitride ALD films, which could be the major factor in the improved uniformity of the films in this study.

The variation in T_c could also be attributed to thickness variation across the wafer. From the ellipsometry data in figure 1(a), we observe an increase in film thickness of 3 Å from the wafer centre to the wafer edge.

Table 2. Variation of NbN PEALD film properties across 200 mm wafer diameter: $d = 8.0$ nm (240 cycles).

Parameter	Centre value (position (0, 0))	Change over 100 mm (%)	Change over 200 mm (%)
T_c (K)	11.1	+4.5	+6.3
ΔT_c (K)	0.64	+25	+33
R_s (Ω/\square)	204.6	-3.3	-9.9
J_c (MA cm^{-2})	10.2	-39	-51
RRR (a.u.)	1.08	<1	<1
R_q (nm)	0.44	+11	+23

This would only explain a minimal increase in T_c , as from the results summarised in table 1, the difference in T_c observed from $d = 5.9$ nm to $d = 8$ nm is 0.8 K. Consequently, the maximum change in T_c across the wafer of 0.9 K cannot purely be related to variation in film thickness. We have also examined the surface roughness across the wafer to understand if morphological changes across the wafer have contributed to the change in T_c , with the root mean squared surface roughness, R_q , for the sample at position (0, 0) being measured as 0.44 nm. Figure 3(d) shows the surface roughness scan for the sample at position (0, 0) measured using AFM. This is significantly lower than what has been reported by Knehr *et al*, however, we report a greater increase in surface roughness across the wafer area, with an 11% and 23% increase in R_q at 100 mm and 200 mm respectively. We also report a superior variation in ΔT_c to the previous study by Knehr, with a 25% increase across a 100 mm range compared to 30%. We observe a variation in ΔT_c across a 200 mm range of 33%, indicating further degradation of film homogeneity approaching the wafer edge, likely a consequence of the plasma source geometry. However, the increase in R_q from the wafer centre to edge could also be a factor in the increase in ΔT_c . It is likely that there is also a structural factor contributing to the variation in superconducting and electrical properties, however, we have yet to examine the variation in lattice parameter across the sample area that has been described in previous works.

Transport measurements on microbridge structures were performed at varying temperatures, ranging from 2.6 K to 9.5 K (just below the measured T_c of the microbridge) with the results fitted using the Bardeen equation [33]:

$$J_c(T) = J_c(0) \times \left[1 - \left(\frac{T}{T_c} \right)^2 \right]^{3/2} \quad (3)$$

where $J_c(T)$ is the measured J_c at temperature T and $J_c(0)$ is the J_c at 0 K, extracted from the fit of $J_c(T)$ to equation (3). $J_c(0)$ and T_c are used as the fitting parameters. The current versus voltage (IV) characteristics were measured to determine the I_c , with J_c then determined by dividing the I_c by the cross-sectional area of the microbridge (film thickness multiplied by the bridge width). Figure 4(c) shows the design of the microbridge structure graphic data system (GDS) file, with an optical microscope image of the fabricated bridge in the zoomed inset. Figures 4(a) and (b) show the J_c versus T data, fit with equation (3), for microbridges fabricated on samples (0, 0) and (0, 3) respectively. For the sample at (0, 0) we observe $J_c = 10.2 \text{ MA cm}^{-2}$ at 2.6 K, with the fit to equation (3) yielding $J_c(0) = 10.9 \text{ MA cm}^{-2} \pm 0.19$ and $T_c = 10.2 \text{ K} \pm 0.33$. Overall, this shows good agreement with equation (3) across the full temperature range recorded from 2.6 K to 9.6 K.

We observe a decrease in the measured J_c of 39% and 51%, respectively, as we move 100 mm and 200 mm from the wafer centre. This indicates a degradation in film quality and cannot be explained by variations in the microbridge fabrication process. The previous study by Knehr *et al* showed a maximum recorded $J_c = 5.7 \text{ MA cm}^{-2}$ at 4.2 K, with J_c versus temperature diverging from equation (3) at temperatures below $0.8T_c$, likely due to vortex entry [17]. The magnetic shielding in our setup is most probably responsible for the J_c versus temperature data better adhering to equation (3) for the microbridges in this study. Overall, this shows that RF substrate biasing can enhance J_c compared to films grown using a standard PEALD process. J_c of films grown via our PEALD process also compare well to sputtered films, with $d = 10$ nm NbN grown on Si exhibiting $J_c(0)$ of $<4 \text{ MA cm}^{-2}$ [34]. 8 nm sputtered NbN on sapphire was reported as having $J_c(0)$ of 11.5 MA cm^{-2} [28], which is expected to be higher than our PEALD process due to the superior lattice matching of the substrate.

The theoretical depairing current density $J_{\text{dep}}(0)$ is given by following relation, derived from work by Clem and Kogan [35]:

$$J_{\text{dep}}(0) = 1.491N(0)e[\Delta(0)]^{3/2}\sqrt{D/\hbar} \quad (4)$$

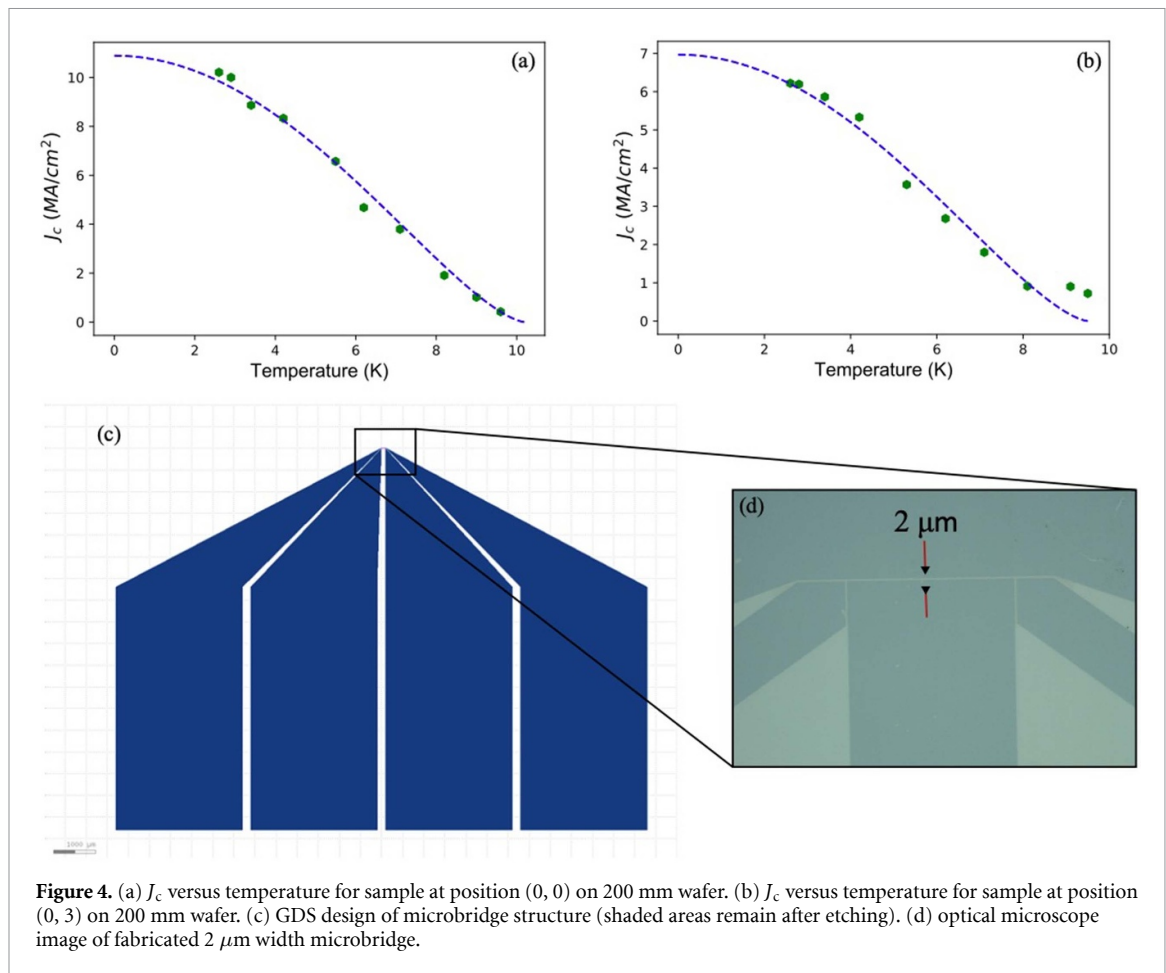
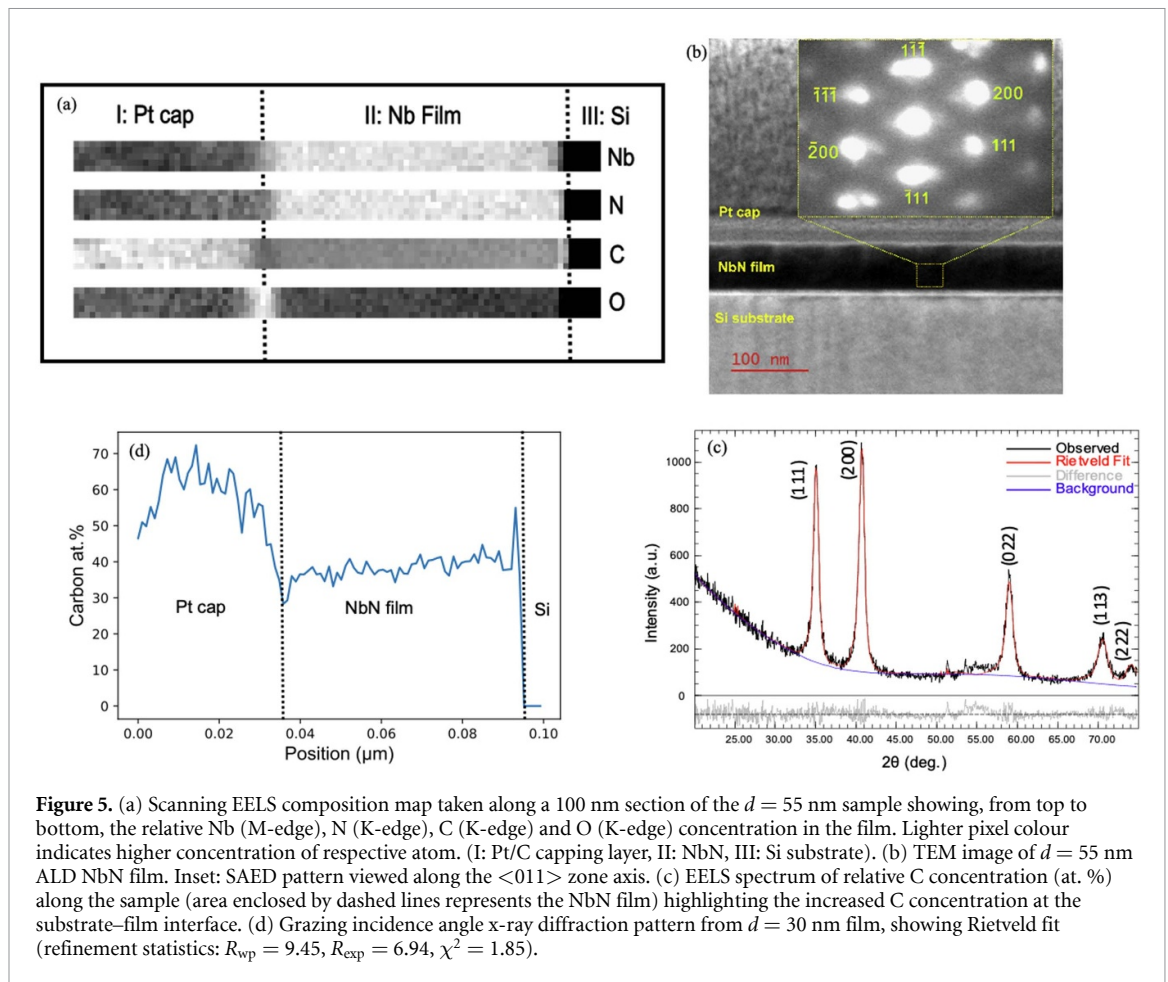


Figure 4. (a) J_c versus temperature for sample at position (0, 0) on 200 mm wafer. (b) J_c versus temperature for sample at position (0, 3) on 200 mm wafer. (c) GDS design of microbridge structure (shaded areas remain after etching). (d) optical microscope image of fabricated $2\ \mu\text{m}$ width microbridge.

where the density of states $N(0) = 1/(2e^2\rho D)$, the energy gap $\Delta(0) = 2.05k_bT_c$ [36], e is the electron charge, k_b is the Boltzmann constant and D is the electron diffusion constant for the NbN film. Using the experimentally recorded values of ρ and T_c , and an estimate of $D = 0.5\ \text{cm}^2\ \text{s}^{-1}$, taken from the literature, we calculate $J_{\text{dep}}(0) = 21.64\ \text{MA}\ \text{cm}^{-2}$ for position (0, 0). By examining the ratio $J_c(0)/J_{\text{dep}}(0)$ we can assess the relationship between J_c , T_c and ρ , with the value of $J_c(0)/J_{\text{dep}}(0)$ for the sample at position (0, 0) = 0.51, slightly lower than what has been reported in previous studies [17, 37]. We observe a marked decrease in $J_c(0)/J_{\text{dep}}(0)$ as we move to the wafer edges, with $J_c(0)/J_{\text{dep}}(0) = 0.16$ at position (0, 6). This indicates J_c does not scale proportionally to $T_c^{3/2}/\rho$, meaning we cannot explain the observed variation in $J_c(0)/J_{\text{dep}}(0)$ by the measured changes in T_c and ρ . It is likely that the value of D is not constant throughout the film, as from the relation $N(0) = 1/(2e^2\rho D)$ we would expect the value of D to increase in our samples, as ρ decreases from the wafer centre to wafer edge by $\sim 10\%$. This would result in an increase in the theoretical $J_{\text{dep}}(0)$ value, consequently explaining the observed decrease in $J_c(0)/J_{\text{dep}}(0)$ from wafer centre to wafer edge. The expected increase in D at the wafer edge could be explained by an increase in Nb content in the film, in keeping with the observed decrease in ρ , as reported by Henrich *et al* in their study of sputtered NbN films [38]. Further investigation is planned to directly measure D for the films in this study, as well as to map the variation across the wafer area to test the assumption that changes in D are responsible for the decrease in $J_c(0)/J_{\text{dep}}(0)$.

3.3. Structure and composition of ALD NbN thin films

It is likely the observed variation in J_c is a result of structural variations across the film area, as observed in previous studies [17, 20]. Therefore, we have examined the structure and composition of the samples in this study using both x-ray diffraction and electron beam diffraction. Figure 5 summarises the structural and compositional study. TEM images from a $d = 55\ \text{nm}$ sample deposited using the same recipe as the aforementioned samples are shown in figure 5(b), with selected area electron diffraction pattern shown in the inset. The diffractogram in figure 5(b) shows the presence of (111) and (200) crystal orientations consistent with δ -NbN (viewed through the $\langle 011 \rangle$ zone axis). STEM electron energy loss spectroscopy (EELS) was acquired with a JEOL ARM200cF, equipped with a Gatan 965 Quantum ER spectrometer. An acceleration voltage of 200 kV was used. Analysis was undertaken within the *Digital Micrograph^h*™ software package, following standard processing steps, including Fourier-log deconvolutions to remove the effects of plural



scattering. Figure 5(a) shows four EELS composition maps from a $4 \text{ nm} \times 100 \text{ nm}$ scan across a cross-section of deposited NbN film. They highlight the relative concentration of Nb, N, C and O in different regions across the sample cross-section. As expected, there is a significant Nb and N content in the film, however, it has been shown that there is also significant C content, notably at the substrate–film interface. This has been previously shown for PEALD of NbN and other materials, such as TaN [3, 39]. Figure 5(c) shows the variation in the C atom % across the film, highlighting the increase in C at the substrate–film interface. It has been well documented that C is incorporated into PEALD NbN films, originating from the organic ligands in the TBTDEN precursor, however, previous studies show C concentration in the film of 12% or less [3, 40]. EELS data from the films in this study indicate a C concentration of $\sim 30\%$, potentially indicating the presence of NbC in the film. This was verified by further analysis on $d = 29.8$ nm sample. NbC is also a superconductor, with bulk T_c of the cubic phase ~ 12 K, as well as an amorphous phase with $T_c < 2$ K [41]. From the diffraction pattern in figure 5(b), we observe what appears to be the presence of overlapping diffraction spots. These artefacts could potentially be a result of stacking faults or lattice defects, however, it could also be indicative of the presence of cubic NbC, which has a similar lattice parameter, a , to δ -NbN; $a = 4.51 \text{ \AA}$ for NbC compared to $a = 4.45 \text{ \AA}$ for NbN. NbC crystallites of the same orientation as those for NbN would therefore show diffraction spots at similar angles, leading to potential overlap. The coexistence of NbC could also be used to explain the observed decrease in $J_c(0)/J_{dep}(0)$ discussed previously, as NbC has shown to have D values roughly one order of magnitude higher ($5\text{--}8 \text{ cm}^2 \text{ s}^{-1}$) than that of NbN [42]. Further work is planned to map the C content across the 200 mm wafer using EELS to probe this hypothesis.

As the purity of a thin film is generally a key consideration for any application, it would be useful to be able to accurately and conclusively characterise this using EELS data. While the EELS data acquired here allows for composition estimations to be made and some conclusions to be drawn alongside the other quantitative analysis methods used, there are well-established errors to be considered. The Hartree–Slater atomic wave function model was used and assumes a spherical, isolated atom, though does not account for bonding or crystallinity. These do, however, affect electron scattering, and thus the calculated composition of the sample, meaning accurate elemental quantification can be difficult, particularly where M-edge transitions are considered, as in the case of Nb here.

Table 3. Peak 2θ position, FWHM and area for the XRD pattern of the $d = 29.8$ nm (1500 cycles) sample.

Orientation (hkl)	2θ ($^\circ$)	FWHM ($^\circ$)	Peak area (a.u.)
(111)	35.2	0.75	821.3
(200)	40.9	0.81	1022.1
(022)	59.2	0.97	487.8
(113)	70.7	1.27	256.0
(222)	74.2	1.04	91.7

To further investigate structure and composition, we have examined a $d = 29.8$ nm sample using x-ray diffractometry to explore the structure and phase purity of the films. Figure 5(d) shows the diffraction pattern, with a Rietveld structural refinement on the diffraction pattern being performed. Initial indexing reaffirmed the presence of (111) and (200) oriented grains typical of δ -NbN, at 35.2° and 40.9° respectively. The peak area ratio, (111)/(200), is measured as 0.80, showing the dominance of (200) grain orientation, similar to what has been reported in previous studies [17]. The full width at half maximum (FWHM) of the (111) and (200) peaks are 0.75° and 0.81° , respectively, narrower than what has been reported in previous PEALD NbN studies [17]. This further strengthens the argument for the use of RF substrate biasing in enhancing the crystallinity of NbN thin films. However, peak broadening in XRD peaks can arise from myriad factors, such as crystallite size, defects (stacking faults, twin faults), or lattice distortion (microstrain), as well as instrumental contributions [43]. We also observe three further peaks at 59.2° , 70.7° and 74.2° that can be attributed to grains of (022), (113) and (222) orientation. This confirms the polycrystalline nature of the films and shows a non-ideal lattice parameter, with peak positions offset relative to the ideal for an $a = 4.45$ Å δ -NbN lattice. The mean crystallite size was determined as 11.7 nm using the Scherrer equation, from the (111) FWHM. Table 3 summarises the XRD results for the $d = 29.8$ nm sample.

The presence of slight peak broadening at the base of the (111), (200) and (022) peaks led to exploring the coexistence of other materials/phases through performing Rietveld structural refinements on the diffraction patterns. Given its structural similarity to δ -NbN, cubic NbC also has XRD peaks located at similar 2θ values, making it an ideal candidate to run in structural refinement. Initial refinement using purely an NbN structural model gave $\chi^2 > 5$, with the value converging to ~ 2 after including NbC structure, strengthening the argument for its presence in our films. The refined lattice parameters for NbN and NbC were: $a = 4.42$ Å and $a = 4.55$ Å respectively. Evidence of a further small diffraction peak at 51.5° consistent with tetragonal NbO₂ indicated its presence in the film, with inclusion in the refinement model leading to a further convergence of χ^2 to 1.9. The presence of the small amount of NbO₂ is likely from native oxide formation on the top surface resulting from post-processing, as indicated by the scanning EELS maps. However, it is likely that there does exist a minute fraction of niobium oxide or oxynitride phases within the film, as indicated by previous works on PEALD of NbN thin films [3, 40].

4. Conclusion

We have investigated the superconducting, morphological and electrical properties of PEALD NbN, showing there to be a negligible variation in the T_c across a 200 mm area ($<7\%$). Variation in the J_c across the wafer area was in line with previously reported studies, exhibiting a 39% decrease across a 100 mm area. Analysis of the theoretical depairing current density, $J_{\text{dep}}(0)$, indicates structural changes across the film are likely responsible for the variation in J_c , with the measured variation in T_c and ρ unable to explain the decrease in measured J_c moving to the wafer edges. EELS and XRD analysis, coupled with T_c and ΔT_c data, has indicated the coexistence of superconducting NbC within the film, however, further work is required to understand the exact film stoichiometry and how this changes as a function of film thickness and across the sample area.

Overall, we have shown that PEALD of NbN using RF substrate biasing can produce highly uniform superconducting NbN films at relatively low temperatures (250°C) over large areas, with minimal drop-off in T_c over a 200 mm range. This has the potential to replace magnetron sputtering as the standard thin film deposition technique for superconducting thin films for emerging photonic quantum technologies such as SNSPDs. This work has the potential to enable the fabrication of large-scale arrays of SNSPDs with high yield and uniform, consistent device performance, compatible with large scale hybrid integration for quantum photonics [44]. This improved thin film technology could have a profound effect on burgeoning SNSPD application areas including integrated receivers for multichannel quantum key distribution [45], satellite quantum key distribution receivers [46], large scale photonic quantum computing [47, 48], superconducting optoelectronic circuits for neuromorphic computing [49], SNSPD receivers for single-photon LIDAR [50] and advanced SNSPD detectors for dark matter searches [51].

Data availability statement

All data that support the findings of this study are included within the article (and any supplementary files).

Acknowledgments

We would like to thank Mr C How and Mr B Smith of the Kelvin Nanocharacterisation Centre (University of Glasgow) for their assistance in T E M sample preparation and imaging. R H H acknowledges support from UK Research and Innovation Grants ST/T005920/1, EP/T00097X/1 and EP/S026428/1. C T L acknowledges a PhD studentship sponsored by Oxford Instruments Plasma Technology and is supported by the EPSRC Centre for Doctoral Training in Intelligent Sensing and Measurement, Grant Number EP/L016753/1.

ORCID iDs

C T Lennon  <https://orcid.org/0000-0001-5057-481X>

Y Shu  <https://orcid.org/0009-0007-6492-9440>

J C Brennan  <https://orcid.org/0009-0009-8009-4935>

D K Namburi  <https://orcid.org/0000-0003-3219-2708>

L A Longchar  <https://orcid.org/0000-0003-1561-0330>

S Srinath  <https://orcid.org/0000-0002-9585-0467>

R H Hadfield  <https://orcid.org/0000-0002-8084-4187>

References

- [1] Richey N E, De Paula C and Bent S F 2020 Understanding chemical and physical mechanisms in atomic layer deposition *J. Chem. Phys.* **152** 040902
- [2] Profijt H B, Potts S E, van de Sanden M C M and Kessels W M M 2011 Plasma-assisted atomic layer deposition: basics, opportunities, and challenges *J. Vac. Sci. Technol. A* **29** 050801
- [3] Sowa M J, Yemane Y, Zhang J, Palmstrom J C, Ju L, Strandwitz N C, Fritz B, Provine J and Prinz F B 2017 Plasma-enhanced atomic layer deposition of superconducting niobium nitride *J. Vac. Sci. Technol. A* **143** 01B143
- [4] George S M 2010 Atomic layer deposition: an overview *Chem. Rev.* **110** 111–31
- [5] Morozov D V, Casaburi A and Hadfield R H 2021 Superconducting photon detectors *Contemp. Phys.* **62** 69–91
- [6] Sheagren C, Barry P, Shirokoff E and Tang Q Y 2020 Atomic layer deposition niobium nitride films for high-Q resonators *J. Low Temp. Phys.* **199** 875–82
- [7] Morozov D, Doyle S M, Banerjee A, Brien T L R, Hemakumara D, Thayne I G, Wood K and Hadfield R H 2018 Design and characterisation of titanium nitride subarrays of kinetic inductance detectors for passive terahertz imaging *J. Low Temp. Phys.* **193** 196–202
- [8] Dineen M *et al* 2020 Atomic layer deposition for quantum devices (White Paper) (available at: <https://plasma.oxinst.com/media-centre/wp/ald-for-quantum-devices>)
- [9] Banerjee A, Heath R M, Morozov D, Hemakumara D, Nasti U, Thayne I and Hadfield R H 2018 Optical properties of refractory metal based thin films *Opt. Mater. Express* **9** 2072–88
- [10] Hadfield R H, Leach J, Fleming F, Paul D J, Tan C H, Ng J S, Henderson R K and Buller G S 2023 Single-photon detection for long-range imaging and sensing *Optica* **10** 1124
- [11] Natarajan C M, Tanner M G and Hadfield R H 2012 Superconducting nanowire single-photon detectors: physics and applications *Supercond. Sci. Technol.* **25** 063001
- [12] Korzh B *et al* 2020 Demonstration of sub-3 ps temporal resolution with a superconducting nanowire single-photon detector *Nat. Photon.* **14** 250–5
- [13] Chang J *et al* 2021 Detecting telecom single photons with 99.5–2.07+0.5% system detection efficiency and high time resolution *APL Photon.* **6** 036114
- [14] Esmail Zadeh I, Chang J, Los J W N, Gyger S, Elshaari A W, Steinhauer S, Dorenbos S N and Zwiller V 2021 Superconducting nanowire single-photon detectors: a perspective on evolution, state-of-the-art, future developments, and applications *Appl. Phys. Lett.* **118** 190502
- [15] Ilin K, Schneider R, Gerthsen D, Engel A, Bartolf H, Schilling A, Semenov A, Huebers H-W, Freitag B and Siegel M 2008 Ultra-thin NbN films on Si: crystalline and superconducting properties *J. Phys.: Conf. Ser.* **97** 012045
- [16] Cucciniello N, Lee D, Feng H Y, Yang Z, Zeng H, Patibandla N, Zhu M and Jia Q 2022 Superconducting niobium nitride: a perspective from processing, microstructure, and superconducting property for single photon detectors *J. Phys.: Condens. Matter* **34** 374003
- [17] Knehr E, Ziegler M, Linzen S, Ilin K, Schanz P, Plentz J, Diegel M, Schmidt H, Il'ichev E and Siegel M 2021 Wafer-level uniformity of atomic-layer-deposited niobium nitride thin films for quantum devices *J. Vac. Sci. Technol. A* **39** 052401
- [18] Cheng R, Wang S and Tang H X 2019 Superconducting nanowire single-photon detectors fabricated from atomic-layer-deposited NbN *Appl. Phys. Lett.* **115** 241101
- [19] Ukibe M and Fujii G 2017 Superconducting characteristics of NbN films deposited by atomic layer deposition *IEEE Trans. Appl. Supercond.* **27** 1–4
- [20] Linzen S, Ziegler M, Astafiev O V, Schmelz M, Hübner U, Diegel M, Il'ichev E and Meyer H-G 2017 Structural and electrical properties of ultrathin niobium nitride films grown by atomic layer deposition *Supercond. Sci. Technol.* **30** 035010
- [21] Yemane Y T, Sowa M J, Zhang J, Ju L, Deguns E W, Strandwitz N C, Prinz F B and Provine J 2017 Superconducting niobium titanium nitride thin films deposited by plasma-enhanced atomic layer deposition *Supercond. Sci. Technol.* **30** 095010

- [22] Knehr E, Kuzmin A, Vodolazov D Y, Ziegler M, Doerner S, Ilin K, Siegel M, Stolz R and Schmidt H 2019 Nanowire single-photon detectors made of atomic layer-deposited niobium nitride *Supercond. Sci. Technol.* **32** 125007
- [23] Taylor G G, Morozov D V, Lennon C T, Barry P S, Sheagren C and Hadfield R H 2021 Infrared single-photon sensitivity in atomic layer deposited superconducting nanowires *Appl. Phys. Lett.* **118** 191106
- [24] Doebelin N and Kleeberg R 2015 Profex: a graphical user interface for the Rietveld refinement program BGMN *J. Appl. Crystallogr.* **48** 1573–80
- [25] Giannuzzi L A and Stevie F A 1999 A review of focused ion beam milling techniques for TEM specimen preparation *Micron* **30** 197–204
- [26] Medeiros O, Colangelo M, Charaev I and Berggren K K 2019 Measuring thickness in thin NbN films for superconducting devices *J. Vac. Sci. Technol. A* **37** 041501
- [27] Mei A B, Howe B M, Zhang C, Sardela M, Eckstein J N, Hultman L, Rockett A, Petrov I and Greene J E 2013 Physical properties of epitaxial ZrN/MgO(001) layers grown by reactive magnetron sputtering *J. Vac. Sci. Technol. A* **31** 061516
- [28] Semenov A *et al* 2009 Optical and transport properties of ultrathin NbN films and nanostructures *Phys. Rev. B* **80** 054510
- [29] Shiino T, Shiba S, Sakai N, Yamakura T, Jiang L, Uzawa Y, Maezawa H and Yamamoto S 2010 Improvement of the critical temperature of superconducting NbTiN and NbN thin films using the AlN buffer layer *Supercond. Sci. Technol.* **23** 045004
- [30] Ivry Y, Kim C, Dane A E, De Fazio D and McCaughan A 2014 Universal scaling of the critical temperature for thin films near the superconducting-to-insulating transition *Phys. Rev. B* **90** 1–23
- [31] Simonin J 1986 Surface term in the superconductive Ginzburg-Landau free energy: application to thin films *Phys. Rev. B* **33** 7830–2
- [32] Faraz T *et al* 2018 Tuning material properties of oxides and nitrides by substrate biasing during plasma-enhanced atomic layer deposition on planar and 3D substrate topographies *ACS Appl. Mater. Interfaces* **10** 13158–80
- [33] Bardeen J 1962 Critical fields and currents in superconductors *Rev. Mod. Phys.* **34** 667–81
- [34] Il'in K, Siegel M, Engel A, Bartolf H, Schilling A, Semenov A and Huebers H-W 2008 Current-induced critical state in NbN thin-film structures *J. Low Temp. Phys.* **151** 585–90
- [35] Clem J R and Kogan V G 2012 Kinetic impedance and depairing in thin and narrow superconducting films *Phys. Rev. B* **86** 1–16
- [36] Pracht U S *et al* 2013 Electrodynamics of the superconducting state in ultra-thin films at THz frequencies *IEEE Trans. Terahertz Sci. Technol.* **3** 269–80
- [37] Frasca S *et al* 2019 Determining the depairing current in superconducting nanowire single-photon detectors *Phys. Rev. B* **100** 1–7
- [38] Henrich D, Dörner S, Hofherr M, Il'in K, Semenov A, Heintze E, Scheffler M, Dressel M and Siegel M 2012 Broadening of hot-spot response spectrum of superconducting NbN nanowire single-photon detector with reduced nitrogen content *J. Appl. Phys.* **112** 1–15
- [39] Peeters S A, Lennon C T, Merckx M J M, Hadfield R H, Kessels W M M, Verheijen M A and Knoops H C M 2023 Ultrathin superconducting TaC_xN_{1-x} films prepared by plasma-enhanced atomic layer deposition with ion-energy control *Appl. Phys. Lett.* **123** 132603
- [40] Deguns E, Sowa M, Dalberth M, Bhatia R, Kanjolia R, Moser D, Sundaram G and Becker J 2010 Plasma-enabled ALD of niobium nitride with organometallic Nb precursors *ECS Meet. Abstr.* **MA2010-02** 1418
- [41] Klug J A, Proslie T, Elam J W, Cook R E, Hiller J M, Claus H, Becker N G and Pellin M J 2011 Atomic layer deposition of amorphous niobium carbide-based thin film superconductors *J. Phys. Chem. C* **115** 25063–71
- [42] Karasik B S, Il'in K S, Pechen E V and Krasnosvobodtsev S I 1996 Diffusion cooling mechanism in a hot-electron NbC microbolometer mixer *Appl. Phys. Lett.* **68** 2285–7
- [43] Ungár T 2004 Microstructural parameters from x-ray diffraction peak broadening *Scr. Mater.* **51** 777–81
- [44] Elshaari A W, Pernice W, Srinivasan K, Benson O and Zwiller V 2020 Hybrid integrated quantum photonic circuits *Nat. Photon.* **14** 285–98
- [45] Terhaar R *et al* 2023 Ultrafast quantum key distribution using fully parallelized quantum channels *Opt. Express* **31** 2675
- [46] You L *et al* 2018 Superconducting nanowire single photon detection system for space applications *Opt. Express* **26** 2965
- [47] Rudolph T 2017 Why I am optimistic about the silicon-photonics route to quantum computing *APL Photon.* **2** 030901
- [48] Wang J, Sciarrino F, Laing A and Thompson M G 2020 Integrated photonic quantum technologies *Nat. Photon.* **14** 273–84
- [49] Khan S *et al* 2022 Superconducting optoelectronic single-photon synapses *Nat. Electron.* **5** 650–9
- [50] Taylor G G, Morozov D, Gemmell N R, Erotokritou K, Miki S, Terai H and Hadfield R H 2019 Photon counting LIDAR at 2.3 μm wavelength with superconducting nanowires *Opt. Express* **27** 38147
- [51] Hochberg Y, Charaev I, Nam S-W, Verma V, Colangelo M and Berggren K K 2019 Detecting sub-GeV dark matter with superconducting nanowires *Phys. Rev. Lett.* **123** 151802